Inverse scheme for sound localization

Jonathan Nowak[1], Stefan Gombots[1], Manfred Kaltenbacher[1,2], Barbara Kaltenbacher[3]
[1] TU Wien, Österreich, Email: (jonathan.nowak, stefan.gombots, manfred.kaltenbacher)@tuwien.ac.at
[2] TU Graz, Österreich, Email: manfred.kaltenbacher@tugraz.at
[3] Alpen-Adria-Universität Klagenfurt, Österreich, Email: Barbara.Kaltenbacher@aau.at

Introduction

Sound source localization with microphone array measurements is widely used e. g. for error detection or improvements of products concerning their acoustic properties. Advantages are that common algorithms such as Conventional Beamforming [1], Functional Beamforming [2] or deconvolution techniques (e. g. CLEAN-SC [3]) are robust and fast. Disadvantages are that these methods are limited in the lower frequency range, usually free radiation is assumed and only the amplitude of sound sources can be recovered. Results of these methods are maps of the acoustic source strength (or sometimes the acoustic pressure) plotted in one plane.

In [4] an inverse scheme using microphone array measurements and finite element simulations was introduced. An extension to this scheme is presented so that sound sources on surfaces are modeled as vibrating surfaces, i. e. the normal component of the acoustic particle velocity is identified in amplitude and phase.

Inverse Scheme

The inverse problem as presented in [4] is to reconstruct sound sources from microphone measurements p_i^{ms}. The underlying idea of the presented method is to match the acoustic pressure of a measurement and a finite element simulation at M certain microphone positions. In other words the error between the measured acoustic pressure p_i^{ms} and computed acoustic pressure p_{a}, both evaluated at the discrete microphone positions $\boldsymbol{x}_i$, is minimized.

We assume that the original geometry of the setup and Fourier-transformed acoustic pressure signals $p_i^{\mathrm{ms}}(\omega)$ ($i = 1, ..., M$) are given. We define a domain Ω that consists of a domain $\Omega_{\mathrm{acou}} \subset \Omega$ and $\Omega_{\mathrm{sc}} \subseteq \Omega_{\mathrm{acou}}$. We assume the sound sources to be located in Ω_{sc} and on $\partial\Omega_{\mathrm{sc}}$ and the microphones to be at positions $\boldsymbol{x}_i \in \Omega_{\mathrm{acou}}$, see Fig. 1. At the outer boundary $\partial\Omega$ we can either apply sound hard boundary conditions that lead to full reflection or we apply boundary conditions that lead to – in practice more realistic – partial reflections. This can be accomplished e. g. by applying impedance boundary conditions or by modeling acoustic absorbers as a separate region as an equivalent fluid with complex material properties [5].

The forward problem in its strong form is defined in frequency domain as

$$\nabla \cdot \nabla p_{\mathrm{a}} + k^2 p_{\mathrm{a}} = \sigma \quad \text{in } \Omega, \tag{1}$$

also known as the Helmholtz equation. The reconstruction of sound sources is performed for a fixed angular sound frequency ω. In Eq. (1) p_{a} denotes the acoustic pressure, $k = \omega/c_0$ the wave number whereby c_0 is the speed of sound. The modeling of sound sources σ on the right hand side will be discussed later.

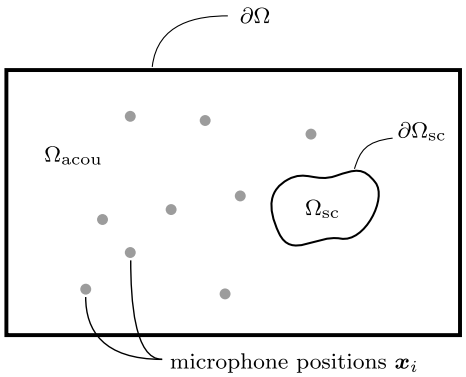

Figure 1: Sketch of the domain Ω.

Since we solve the forward problem via the finite element method, we derive the weak form of Eq. (1) by multiplying with an arbitrary (complex valued) test function p' and integrating by parts

$$\begin{aligned} &\int_\Omega \left(\nabla p_{\mathrm{a}} \cdot \nabla \bar{p}' - k^2 p_{\mathrm{a}} \bar{p}'\right) \mathrm{d}\boldsymbol{x} = \\ &-\int_\Omega \sigma^{\mathrm{in}} \bar{p}' \,\mathrm{d}\boldsymbol{x} + \int_{\partial\Omega} \nabla p_{\mathrm{a}} \bar{p}' \cdot \mathrm{d}\boldsymbol{s} \qquad \forall p' \in V. \end{aligned} \tag{2}$$

Here, σ^{in} are sound sources in the volume and a bar denotes complex conjugation. Further, V denotes the function space of the test functions p', which is a real Hilbert space [4].

Modeling of sound sources

We now want to focus on two different ways of modeling the sound sources. The first approach – referred to case (a) throughout this paper – is to model sources in the volume as well as on the boundary as monopole sources. This leads to the ansatz

$$\sigma^{\mathrm{in}} + \sigma^{\mathrm{bd}} = \sum_{n=1}^{N} a_n \mathrm{e}^{\mathrm{j}\varphi_n} \delta_{\boldsymbol{x}_n}.$$

Here, $N = N^{\mathrm{in}} + N^{\mathrm{bd}}$ the number of possible sources in the domain Ω_{sc} and on its boundary. In the finite element framework N equals the number of nodes in the source region. Further, a_n is the amplitude and φ_n the phase of the n-th sound source and $\delta_{\boldsymbol{x}_n}$ is the delta distribution evaluated at the point of the n-th sound source.

The second approach – called case (b) – models sources at the boundary $\partial\Omega_{\mathrm{sc}}$ as the normal component $v_{\mathrm{n}} = \boldsymbol{v}_{\mathrm{a}} \cdot \boldsymbol{n}$ of the acoustic particle velocity $\boldsymbol{v}_{\mathrm{a}}$. This normal component equals the normal component of the mechanical velocity at $\partial\Omega_{\mathrm{sc}}$ as the interface condition of acoustic particle velocity and mechanic velocity

$$(\boldsymbol{v}_{\mathrm{a}} - \boldsymbol{v}_{\mathrm{m}}) \cdot \boldsymbol{n} = 0 \tag{3}$$

holds. This approach seems to be more appropriate when we think e. g. of reconstructing sound sources at vibrating surface such as a rolling tire.

Due to the linearized equation of mass conservation in time domain

$$\rho_0 \frac{\partial \boldsymbol{v}_{\mathrm{a}}}{\partial t} = -\nabla p_{\mathrm{a}}, \tag{4}$$

with the density ρ_0, we can rewrite the surface integral in Eq. (2), which is in frequency domain, assuming constant density

$$\int_{\partial\Omega} \nabla p_{\mathrm{a}} \bar{p}' \cdot \boldsymbol{n} \,\mathrm{d}s = -\mathrm{j}\omega\rho_0 \int_{\partial\Omega} v_{\mathrm{n}} \bar{p}' \,\mathrm{d}s. \tag{5}$$

This leads to the approach

$$\sigma = \sum_{n=1}^{N^{\mathrm{in}}} a_n \mathrm{e}^{\mathrm{j}\varphi_n} \delta_{\boldsymbol{x}_n} + \mathrm{j}\omega\rho_0 \sum_{m=1}^{N^{\mathrm{bd}}} v_{\mathrm{n},m} \mathrm{e}^{\mathrm{j}\varphi_m} N_m \,. \tag{6}$$

In Eq. (6) $\sigma = \sigma^{\mathrm{in}} + \sigma^{\mathrm{bd}}$ and $N_m(\boldsymbol{x})$ denotes finite element nodal basis functions on Ω satisfying the delta property $N_m(\boldsymbol{x}_n) = \delta_{mn}$.

In order to include also delta pulses, we consider sound sources as elements of the dual space V^*, so that Eq. (2) becomes

$$\begin{aligned} A(p_{\mathrm{a}}, p') \coloneqq \mathrm{Re}\left(\int_{\Omega} \left(\nabla p_{\mathrm{a}} \cdot \nabla \bar{p}' - k^2 p_{\mathrm{a}} \bar{p}' \right) \mathrm{d}\boldsymbol{x} \right) = \\ - \mathrm{Re}\left(\langle \sigma^{\mathrm{in}} + \sigma^{\mathrm{bd}}, \bar{p}' \rangle_{V^*,V} \right) \qquad \forall p' \in V. \end{aligned} \tag{7}$$

Since the imaginary part is redundant, we only consider the real valued problem.

Optimization problem

Fitting of the parameters by means of Tikhonov regularization amounts to solving the constrained optimization problem [4]

$$\begin{aligned} &\min\ J(p,a,\varphi) \quad \text{s.t. } \forall v \in V: \\ &A(p_{\mathrm{a}}, p') = -\mathrm{Re}\left(\sum_{n=1}^{N^{\mathrm{in}}} a_n \mathrm{e}^{\mathrm{j}\varphi_n} \bar{p}'(\boldsymbol{x}_n) \right) \\ &\qquad -\mathrm{Re}\left(\sum_{m=1}^{N^{\mathrm{bd}}} a_m \mathrm{e}^{\mathrm{j}\varphi_m} \langle \mu_m, \bar{p}' \rangle_{V^*,V} \right) \end{aligned} \tag{8}$$

where

$$\mu_m = \begin{cases} \delta_{\boldsymbol{x}_m} & \text{case (a)} \\ \mathrm{j}\omega\rho_0 N_m(\boldsymbol{x}) & \text{case (b)} \end{cases}. \tag{9}$$

The cost functional J is defined as

$$\begin{aligned} J(p,a,\varphi) = \frac{\Phi}{2} \sum_{i=1}^{M} |p_{\mathrm{a}}(\boldsymbol{x}_i) - p_i^{\mathrm{ms}}|^2 \\ + \alpha \sum_{n=1}^{N} |a_n|^q + \beta \sum_{n=1}^{N} \varphi_n^2 \\ - \varrho \sum_{n=1}^{N} \Big(\ln\Big(\frac{\pi}{2} + \varphi_n\Big) + \ln\Big(\frac{\pi}{2} - \varphi_n\Big) \Big), \end{aligned} \tag{10}$$

with appropriately chosen regularization parameters α, β and ϱ. The exponent $q \in (1,2]$ leads to sparse source reconstruction when chosen close to 1. The scaling factor Φ should be chosen appropriately to ensure convergence and avoiding numerical rounding errors. If $\Phi \neq 1$ the identified amplitudes need to be scaled back in order to receive the correct values for the unscaled problem.

We define the following Lagrange functional that reads for case (b) as

$$\begin{aligned} \mathcal{L}(a,\varphi,p,z) = J(p,a,\varphi) + A(p,z) \\ + \mathrm{Re}\left(\sum_{n=1}^{N^{\mathrm{in}}} a_n \mathrm{e}^{\mathrm{j}\varphi_n} \bar{p}'(\boldsymbol{x}_n) \right) \\ + \mathrm{Re}\left(\mathrm{j}\omega\rho_0 \sum_{m=1}^{N^{\mathrm{bd}}} v_{\mathrm{n},m} \mathrm{e}^{\mathrm{j}\varphi_m} \langle N_m, \bar{p}' \rangle_{V^*,V} \right). \end{aligned} \tag{11}$$

The derivation of the calculation of the gradients $\mathrm{d}J/\mathrm{d}a_i$ for case (a) using an adjoint approach can be found in [4] and only minor changes have to be done for case (b).

Numerical Results

For testing purposes a simple 2D example was investigated, see Fig. 2. The computational domain Ω consists of a mechanical domain (green) and an acoustic domain (grey: air, blue: PML), that are coupled via the above mentioned interface condition on Γ_{i} (red), Eq. (3). The region with perfectly matched layer (PML) is used to model free radiation. The mechanical domain is excited with a harmonic force density with $f = 500\,\mathrm{Hz}$ and is clamped at its short sides. In a first case the material parameters are chosen in a way that the plate oscillates at $f = 500\,\mathrm{Hz}$ in its first mode and in a second setup in its third mode. At $\partial\Omega$ sound hard boundary conditions are applied. A regular mesh with linear quadrilateral elements with the size of $h = 0.01\,\mathrm{m}$ was used. Hence, the recommendation of using 10 to 20 linear elements per wave length (see e. g. [6]) is overfulfilled for $f = 500\,\mathrm{Hz}$.

Results for two different microphone arrays were investigated, see Fig. 2. Array 1 is a semicircular array arranged around the oscillating plate, array 2 consists of the same semicircular array with an additional line array.

Identifying the acoustic particle velocity

Results for the two eigenmodes using the two different array configurations depicted in Fig. 2 are shown. The

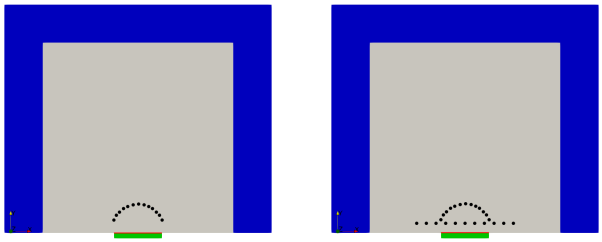

(a) Semicircular array (Array 1).

(b) Semicircular array with line array (Array 2).

Figure 2: Computational domain: mechanical domain (green), air (grey), PML (blue) and interface Γ_i (red).

phase value of the pressure excitation in the mechanic domain is fixed to $\varphi_\mathrm{ex} = -\pi/4$, therefore the phase angle of the velocity is $\varphi = +\pi/4$. All results for the identified and original normal component of the acoustic particle velocity v_n are plotted along the interface Γ_i in amplitude and phase. The values of the forward computation are depicted in blue, the identified values for case (a) are shown in green and for case (b) in orange. In case (a) the values for v_n are calculated as a post processing result, as we identify point sources on the surface, in case (b) the values for v_n are identified directly, so no postprocessing is needed. Therefore the velocity in case (a) is an element result whereas in case (b) it is interpolated between nodes.

Figure 3 shows the identified normal component of the acoustic particle velocity when the plate is oscillating in its first eigenmode. When using only the semicircular array (Fig. 3a), the identified amplitude is underestimated in both cases (a) and (b), whereas results are slightly better in case (b). The results for the amplitude improve in both cases, when using the line array additionally, Fig. 3b. In case (b) the recovered amplitude matches very well. The phase is also reconstructed well. However near the clamped ends it deviates from the forward computation. We want to point out that no additional information such as clamping etc. is used for the inverse computation.

The results for the plate oscillating in its third eigenmode are shown in Fig. 4. The third mode is not identified when using the semicircular array, neither for case (a) nor for case (b). Even if the additional line array is used, the mode is not reconstructed correctly, but in case (b) the amplitude improves slightly.

If we choose a different scaling value Φ for the first term in the cost functional J in Eq. (10), we can improve the identified amplitude in case (b). The phase however worsens, see Fig. 5.

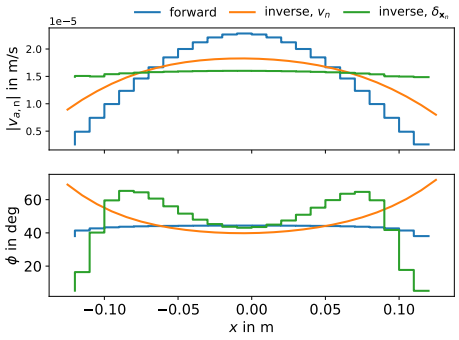

(a) Results for semicircular array.

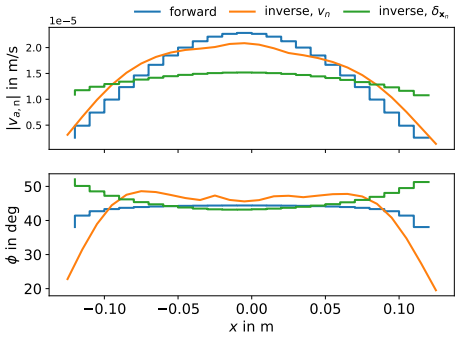

(b) Results for semicircular array with line array.

Figure 3: Results for identified v_n, the plate is oscillating in its first eigenmode; forward calculation (blue), reconstruction case (a) in green and reconstruction case (b) in orange.

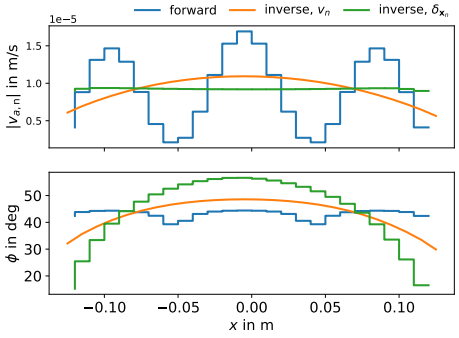

(a) Results for semicircular array.

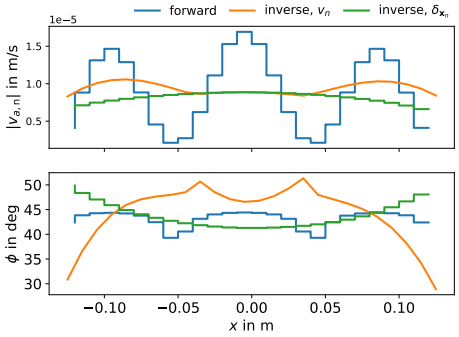

(b) Results for semicircular array with line array.

Figure 4: Results for identified v_n, the plate is oscillating in its third eigenmode; forward calculation (blue), reconstruction case (a) in green and reconstruction case (b) in orange.

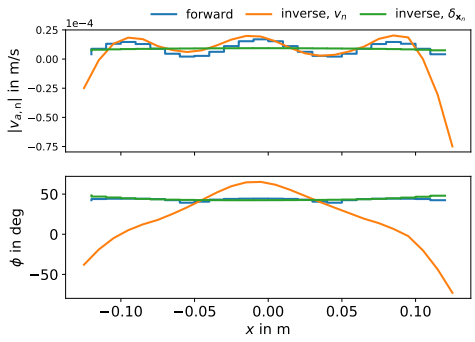

Figure 5: Results for identified v_n with different scaling value in functional J; forward calculation (blue), reconstruction case (a) in green and reconstruction case (b) in orange.

Sound fields

Although the results for the identified acoustic particle velocity are not always correct, the reconstructed sound pressure field is very similar to the one in the forward simulation, see Fig. 6. This demonstrates the ill-posedness of the problem. It also becomes clear, why the third eigenmode is only reconstructed correctly, if we add microphones that are closer to the vibrating beam, as the sound field is only unique in the near field. In the far field the sound pattern that is radiated by the third mode is very similar to the one radiated by the first mode. In practical application this could cause some challenges, as it might not always be possible to place microphones very near to a vibrating object.

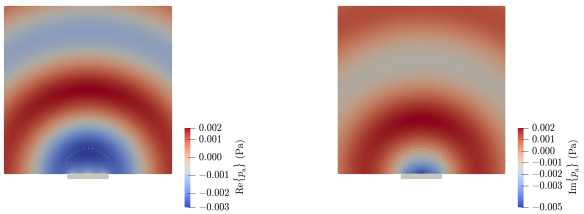

(a) Forward computation: real part of sound pressure.

(b) Forward computation: imaginary part of sound pressure.

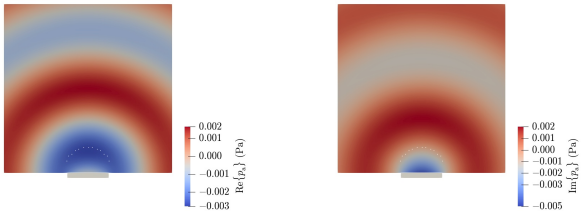

(c) Inverse computation: real part of sound pressure.

(d) Inverse computation: imaginary part of sound pressure.

Figure 6: Real parts of the sound fields in forward and inverse computation (case (b)), excitation with $\varphi_\mathrm{ex} = -45\,\mathrm{deg}$, plate oscilating in its third eigenmode.

Conclusion

An extension to the inverse approach for acoustic source localization using microphone array measurements and finite element simulation was presented. Numerical results of a 2D test example for identifying the normal component of the acoustic particle velocity were presented. This modeling approach is appropriate to model sound sources on vibrating surfaces. Advantages could be shown compared to the case where sound sources on surfaces are modeled as monopole sources. Further investigation need to be done concerning the identification of higher modes of vibrating surfaces, where results are not as good as in case of the first mode. As we only match the simulated sound pressure to the measured sound pressure at discrete microphone positions, they have to be at locations with high sensitivity. Finding the optimal microphone positions will be a task of future research.

References

[1] T. J. Mueller. *Aeroacoustic Measurements*. Springer-Verlag, 2002.

[2] Robert P Dougherty. "Functional beamforming for aeroacoustic source distributions". In: *20th AIAA/CEAS aeroacoustics conference*. 2014, p. 3066.

[3] P. Sijtsma. "CLEAN based on spatial source coherence". In: *Int. J. Aeroacoustics* 6.6 (2009), pp. 357–374.

[4] Manfred Kaltenbacher, Barbara Kaltenbacher, and Stefan Gombots. "Inverse Scheme for Acoustic Source Localization using Microphone Measurements and Finite Element Simulations". In: 2018.

[5] C. Zwikker and C.W. Kosten. *Sound Absorbing Materials*. New York: Elsevier Pub. Co., 1949. ISBN: 978-0-444-40661-3.

[6] M. Kaltenbacher. *Numerical Simulation of Mechatronic Sensors and Actuators: Finite Elements for Computational Multiphysics*. 3rd ed. Springer, 2015.